



Research papers

Modeling of flow and transport in multiscale digital rocks aided by grid coarsening of microporous domains

Bowen Shi^a, Han Jiang^{a,b,*}, Bo Guo^c, Jian Tian^{a,b}, Chao-Zhong Qin^{a,b,*}

^a School of Resources and Safety Engineering, Chongqing University, Chongqing, China

^b State Key Laboratory of Coal Mine Disaster Dynamics and Control, Chongqing University, Chongqing, China

^c Department of Hydrology and Atmospheric Sciences, University of Arizona, Tucson, AZ, USA

ARTICLE INFO

This manuscript was handled by Yuefei Huang, Editor-in-Chief, with the assistance of Delphine Roubinet, Associate Editor

Keywords:

Subsurface porous media
Permeability
Breakthrough curve
Multiscale digital rock
Pore-network-continuum hybrid model
Microporosity

ABSTRACT

Many subsurface porous media such as soils, carbonate rocks, and mudstones possess multiscale porous structures that play an important role in regulating fluid flow and transport therein. A pore-network-continuum hybrid model is promising for numerical studies of a multiscale digital rock. It is, however, still prohibitive to the REV-size modeling because tens of millions of microporosity voxels may exist. In this work, we develop a novel and robust algorithm for coarsening microporosity voxels of a multiscale digital rock. Then, we combine coarsened microporosity grids with the pore network of resolved macropores to form efficient computational meshes. Furthermore, a pore-network-continuum simulator is developed to simulate flow and transport in both a synthesized multiscale digital rock and a realistic Estallades carbonate rock. We show that the coarsening algorithm can reduce computational grids by about 90%, which substantially reduces computational costs. Meanwhile, coarsening microporosity has a minor impact on the predictions of absolute permeability, gas production curves, and breakthrough curves of solute transport. We illustrate the mechanisms of flow and transport in multiscale porous media induced by microporosity. Finally, the efficient hybrid model is used to predict the absolute permeability of an Estallades digital rock. The numerical prediction matches well with the reported experimental data. We highlight the importance of characterizing mean pore-size distributions in microporosity for the prediction of rock permeability and local flow fields. The developed pore-network-continuum hybrid model aided by grid coarsening of microporosity serves as a useful numerical tool to study flow and transport in multiscale porous media.

1. Introduction

With the rapid development of non-invasive imaging techniques and computation performance, Digital Rock Physics (DRP) has been playing an important role in understanding the fundamental physics of flow and transport in porous media (Blunt et al., 2013; Wildenschild & Sheppard, 2013; Qin et al., 2021a, 2022). The most relevant applications include geological sequestration of carbon dioxide (Andrew et al., 2014), underground hydrogen storage (Jangda et al., 2022), contaminant transport in groundwater (Ghareaghloo et al., 2018), and unconventional oil/gas recovery (Guo et al., 2018). Nowadays, from high-resolution images, one can routinely construct realistic porous structures, and conduct pore-scale numerical simulations of material properties such as absolute permeability (Khan et al., 2011; Yang et al., 2019), effective diffusivity (Xu, 2022), capillary pressure (Raeini et al., 2014; Chen et al.,

2020) and relative permeability (Dong & Blunt, 2009; Zhao et al., 2020).

Proper image segmentation of pore spaces is the prerequisite for modeling flow and transport. For rocks with unimodal pore-size distributions, segmentation can be well accomplished, sometimes calibrated by measured porosity. However, many natural rocks present complex and multiscale pore structures, such as soils, carbonate rocks, tight sandstones, and mudstones (Bijeljic et al., 2013; Li et al., 2021; Qin et al., 2021b; Fan et al., 2022; Dai et al., 2023). Extensive Mercury Intrusion Porosimetry (MIP) and Nuclear Magnetic Resonance (NMR) tests have shown bimodal or even multi-modal pore-size distributions of these core samples (Tanino & Blunt, 2012; Nie et al., 2021). Moreover, pore diameters at peak can be different from each other by several orders of magnitude (Lin Ma et al., 2021). Due to the trade-off between image resolution and field of view, it remains prohibitive to obtain a REV-size image with all details of multiscale pore structures. Therefore,

* Corresponding authors at: School of Resources and Safety Engineering, Chongqing University, Chongqing, China.

E-mail addresses: hanjiang_ss@163.com (H. Jiang), chaozhong.qin@cqu.edu.cn (C.-Z. Qin).

in the construction of multiscale digital rocks, the concept of Sub-Resolution Porosity (SRP) (or microporosity), which composes of many micropores that cannot be identified at the current imaging resolution, has been proposed (Soulaine et al., 2016; Guo et al., 2018). In practice, microporosity may be segmented according to the gray values of a dry sample image (Bultreys et al., 2015), or more accurately, based on the image difference between dry and fully-saturated sample scanning (Wang et al., 2022).

When modeling flow and transport in a multiscale digital rock, microporosity may be treated as solid or void spaces by inaccurate segmentation. This can alter the connectivity of pore spaces, and may lead to significant errors in the prediction of flow fields and material properties (Jacob et al., 2021). To address the influences of microporosity on flow and transport, a few hybrid models have been developed in the past few years (Bauer et al., 2012; Soulaine & Tchelepi, 2016; Guo et al., 2018; 2019; Weishaupt & Helmig, 2021; Wu et al., 2022). In general, these models can be classified into two categories: Dual-Pore-Network Models (DPNMs) and micro-continuum models. In a DPNM, microporosity was represented by a fine-scale pore network (Jiang et al., 2013; Mehmani & Prodanović, 2014; Yang et al., 2015; de Vries et al., 2017). However, limited by computation, fine-scale pore networks were numerically generated with a small number of pore elements (Mehmani & Prodanović, 2014). Alternatively, microporosity was represented by the so-called micro-links (Bultreys et al., 2015; Ruspini et al., 2021). In principle, a micro-link was a conceptual porous throat, whose connection with macropores and hydraulic conductivity could be inferred from images. Although this approach considers realistic microporosity distributions, and requires less computation than a traditional DPNM, its accuracy depends on operator-supplied parameters (e.g., micro-link cut-off length). Most recently, Rabbani et al. (Rabbani et al., 2020) presented a triple pore-network model for gas flow in fractured multiscale digital rocks, in which microporosity was discretized by its watersheds. This leads to a network of microporosity elements, which resemble the pore elements of fractures and macropores. To the best of our knowledge, current DPNMs undermine microporosity heterogeneity (e.g., porosity, permeability), which may play an important role in regulating flow and transport.

On the other hand, in a micro-continuum model, flows in microporosity and resolved macropores are respectively described by Darcy's law and Stokes equation. Moreover, the coupling of the two-scale flows is implemented by the well-known Darcy-Brinkman-Stokes equation (Soulaine & Tchelepi, 2016; Guo et al., 2019). Obviously, numerical predictions by micro-continuum models have high fidelity, which can be used to calibrate and verify other numerical models such as DPNMs. However, it is worth noting that micro-continuum models are computationally expensive, and prohibitive to the modeling of a REV-size multiscale digital rock, particularly for the two-phase flow modeling. For instance, for a 200^3 digital rock, it took about 120 h to simulate a two-phase flow process by parallel computation of ten 28-core Broadwell Xeon nodes (Carrillo et al., 2022).

To take advantage of both DPNMs and micro-continuum models, recently, the framework of a pore-network-continuum hybrid model has been proposed and implemented (Zhang et al., 2019; 2023). In this framework, flow and transport in macropores are described by a computationally efficient pore-network model, while a Darcy-scale model is used for microporosity. When microporosity voxels are used as computational grids as usual, computational efforts pertaining to the modeling of microporosity will be prohibitive. This is because tens of millions of voxels of microporosity may present in a standard multiscale digital rock (i.e., 1000^3 voxels). As we know, microporosity may not necessitate high-resolution computational grids, given the fact that gradients of flow and transport in microporosity are much smaller than those in macropores. Therefore, further development of coarsening of the microporosity voxels is promising, and crucial to the application of a pore-network-continuum model.

There have been many studies on voxel-based mesh coarsening, of

which uniformly reducing the image resolution (Maire, 2003) would be the simplest. However, this gives rise to the loss of geometrical details, and thus impacts the accuracy of numerical results (Shah et al., 2016). To solve the issue, coarsening methods based on the quadtree/octree algorithm were used (Legrain et al., 2011; Lei Ma et al., 2023), which can be categorized into coarse-to-fine and fine-to-coarse. The former first extracts smoothed geometrical interfaces of an image. Then, the interfaces are projected onto pre-defined background grids, which are usually quite coarse. The grids intersected with the interfaces are continuously subdivided by the octree algorithm. Finally, a local refinement may be conducted before the tessellation procedure, in order to maintain high resolution of the geometrical interfaces (Verhoosel et al., 2015). This algorithm has been used in many CFD software (e.g., snappyHexMesh in OpenFoam, Adaptive Mesh Refinement in Fluent and Comsol). However, it aims to approach a smooth boundary or interface which may be not necessary to the one represented by voxels. Also, it is worth noting that voxel-representation of boundaries or interfaces is the most accurate for a given CT scanning image. The latter starts with image voxels, and then merges eight grids (or four in 2D), which belong to the same material and have one common node, into one coarsening grid. Multi-level coarsening and smoothening between different levels of coarsening grids can be conducted (Fischer & Eidel, 2020). Although quadtree/octree-based coarsening methods have been widely used in image-based numerical studies (Legrain et al., 2011; Olshanskii et al., 2013; Gackiewicz et al., 2021; Duan et al., 2022; Gote et al., 2022), their application in the problem of flow and transport in a multiscale digital rock has not been reported yet. Regarding the modeling of flow and transport, we need to properly treat the interfaces between macropores and microporosity, and allocate coarsest grids in microporosity regions of low flow gradients, which will be addressed in this work. Moreover, these coarsening methods are usually time-consuming (Friskin & Perry, 2002).

In this work, we develop a novel coarsening algorithm for microporosity voxels, which uses multiple consecutive convolution operations on voxels. The algorithm has the advantages of robustness, high efficiency, and flexible controls on coarsening processes. Together with our in-house pore-network-continuum modeling simulator, a number of case studies including the modeling of absolute permeability, compressible gas production, and solute transport in both a synthesized multiscale digital rock and an Estaillades carbonate rock have been conducted. We analyze the performance of coarsening microporosity in terms of numerical accuracy and computational efficiency, and investigate the effects of microporosity on flow and transport in multiscale porous media.

The remainder of the paper is organized as follows. In Section 2, we present the coarsening algorithm for microporosity voxels in detail, and the generation of computational meshes for our pore-network-continuum modeling simulator. In Section 3, we describe the involved physical models and their numerical implementation. In Section 4, we first show numerical results of flow and transport in an artificial multiscale sample, based on four different types of coarsened grids of microporosity. We then propose an optimal coarsening for microporosity, in order to balance computational efficiency and numerical accuracy. Moreover, we predict the absolute permeability of Estaillades limestone, and compare it with experimental data. Finally, we close with the main conclusions in section 5.

2. Generation of computational meshes

The computational mesh of a multiscale digital rock consists of the pore network of macropores and the grids of microporosity. To reduce computational efforts, we have developed a novel algorithm for generating coarsened computational grids from initial microporosity voxels. In what follows, the pore-network extraction of macropores is presented in Section 2.1; the coarsening of computational grids for microporosity is discussed in Section 2.2; and the fusion of pore network and microporosity grids is given in Section 2.3. Moreover, we use a 2D ternary

image of 40^2 as an example, to help readers understand the generation of computational meshes. As shown in Fig. 1A, the white, the grey, and the black denote void spaces, solid phase, and microporosity, respectively.

2.1. Pore network of macropores

A number of image-based pore-network extraction methods have been reported in the literature (Lindquist et al., 1996; Silin et al., 2003; Dong & Blunt, 2009; Rabbani et al., 2014; Gostick, 2017). In this work, we use the open-source code, PoreSpy, which is built on the watershed segmentation of pore spaces. The key steps involved in the extraction of a pore network are prefiltering the distance map, eliminating saddle and plateau peaks, merging nearby peaks, and segmenting pore spaces into individual pore bodies by using a marker-based watershed (Gostick, 2017).

By PoreSpy, we can obtain the volume, inscribed radius, and surface area of each pore body, the cross-sectional area, inscribed radius, and perimeter of each pore throat, and the connectivity map of pore bodies. We assign all pore volumes to pore bodies, and pore throats are assumed to be volumeless. Fig. 1 shows a 2D schematic of the pore-network extraction. Presume that a segmented ternary image is ready for use. We further process the image to a binarized image in which microporosity is treated as solid phase. Then, the binary image is provided to PoreSpy for the pore-network extraction, while some key parameters (such as Gaussian filter parameter sigma and structuring element size) need to be paid attention to (Gostick, 2017). Finally, the extracted pore network is shown in Fig. 1C.

2.2. Computational grids of microporosity

Instead of directly using microporosity voxels as computational grids, we heavily coarsen microporosity voxels. Here, we first introduce the basic coarsening algorithm. Then, we present three enhanced submodules for potential improvement of mesh quality.

2.2.1. Basic coarsening algorithm

The algorithm proceeds in three main steps: (1) preparing the input image and assigning weight values to its voxels; (2) conducting multiple consecutive convolution operations; and (3) generating and numbering the final computational grids of microporosity.

The flowchart of the basic coarsening algorithm is given in Fig. 2. For a given raw image, we first identify the microporosity by thresholding. We assign weight values of 1 and 0 to the microporosity voxels and the remainder, respectively. Second, we preset the number of convolution operations, N , and their kernels, (k_x^i, k_y^i, k_z^i) , where i is the level index of convolution operation. Usually, we set a cubic kernel with the size of 2^3 ;

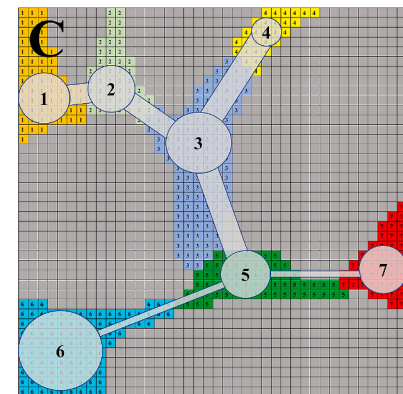
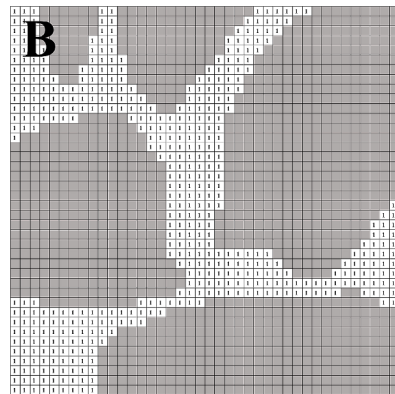
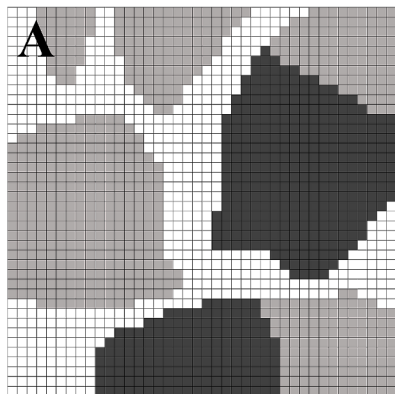


Fig. 1. Schematic of the pore-network extraction. (A) A 2D ternary image of 40^2 pixels. (B) The binarized image as the input to PoreSpy for the pore-network extraction. (C) The extracted pore network with the pore bodies numbered from 1 to 7, while their corresponding watersheds of pixels are also numbered from 1 to 7. In C, the pore bodies are represented by their inscribed circles in 2D.

and the stride is set to the same as the kernel size. After each level of convolution operation, we obtain a new feature map which is axially half the size of the previous feature map. If the weight value in a cell is equal to 8^i (or 4^i for 2D) in the i^{th} level feature map, its projecting microporosity voxels can be coarsened to an i^{th} level computational grid. Before we go into the $(i+1)^{th}$ convolution operation, the weight values smaller than 8^i are reset to 0 in the feature map. It is worth noting that the preset number of convolution operations, N , may not be achieved. The maximum level of convolution operations, however, can be easily determined by weight values in feature maps.

Once all convolution operations are completed, we start with the final level of feature map and loop all the cells along x, y, and z directions in turn, to coarsen and number the microporosity voxels. From the final level of feature map to the input binary image, we sequentially number all the computational grids of microporosity as well as their projecting voxels.

Obviously, each computational grid is linked with its projecting voxels. In such a way, for heterogenous microporosity, we may estimate material properties of a coarsening grid by averaging its projecting voxel values. We notice that if the size of an input image is not an integral multiple of the kernel size, ghost non-microporosity voxels for convolution operations can be added from the boundaries. Meanwhile, versatile coarsening can be conducted by properly designing the kernel size.

To gain an intuitive understanding of the algorithm and its application, the 2D ternary image in Fig. 1A is used as the input image. As shown in Fig. 3A, we assign the weight value of 1 to the microporosity. Fig. 3B-3D shows the feature maps of the three consecutive convolution operations along with weight values in the cells. Fig. 3E shows the final computation grids of the microporosity, which consist of 3 third-level coarsening grids (8×8 voxels) in red, 7 second-level coarsening grids (4×4 voxels) in yellow, 28 first-level coarsening grids (2×2 voxels) in green, and 57 uncoarsened voxel grids, in a total of 95 grids comparing to 473 original microporosity voxels. Notice that we first number pore bodies of the pore network, then computational grids of the microporosity.

2.2.2. Submodules for coarsening controls

One may be aware of that some issues are not addressed yet in the basic coarsening algorithm, such as steep transition between grids and lack of distribution optimization of grids. Therefore, we further develop three most important submodules, namely, transition-layer module, outward-coarsening module, and interface-coarsening module. Together with the basic coarsening algorithm, they can help us improve the mesh quality, and further reduce the number of computational grids of microporosity.

The transition-layer module aims to keep smooth transition between

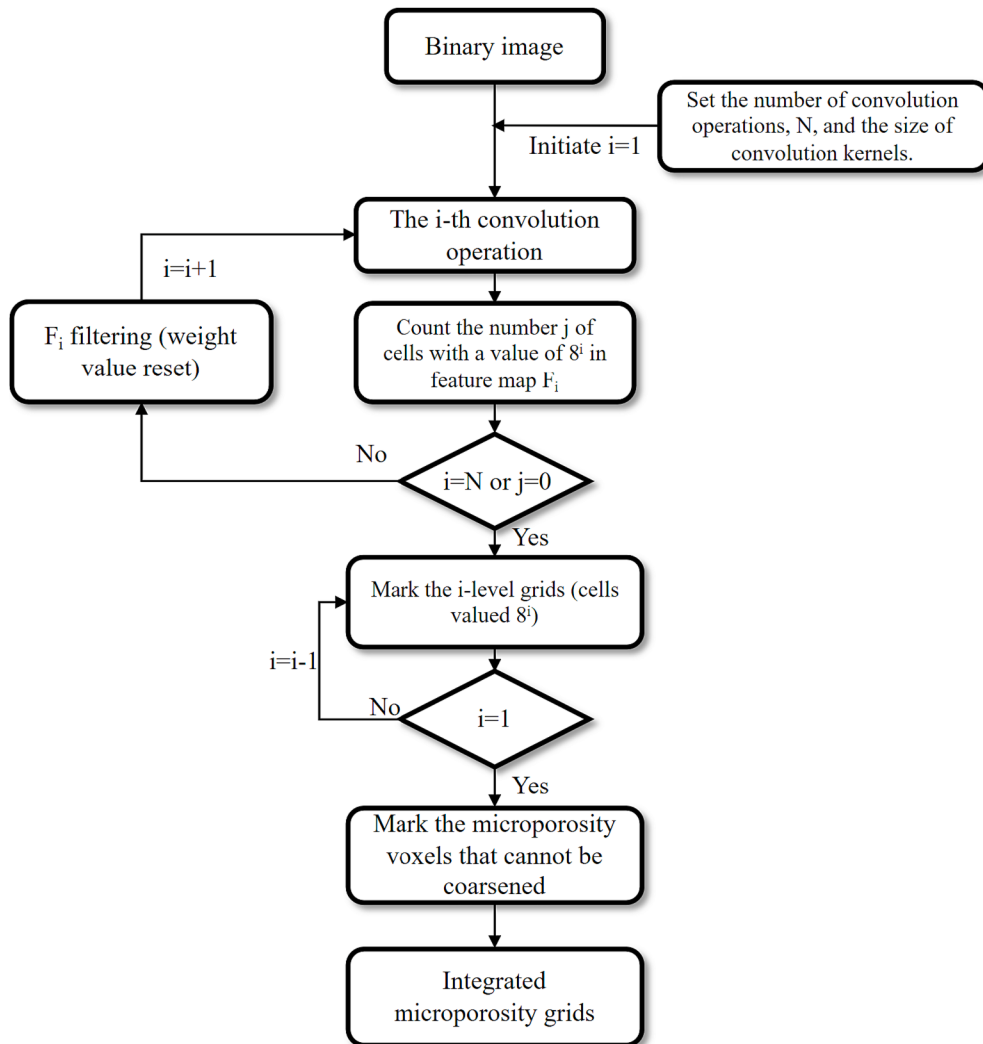


Fig. 2. Flowchart of the basic coarsening algorithm for microporosity voxels.

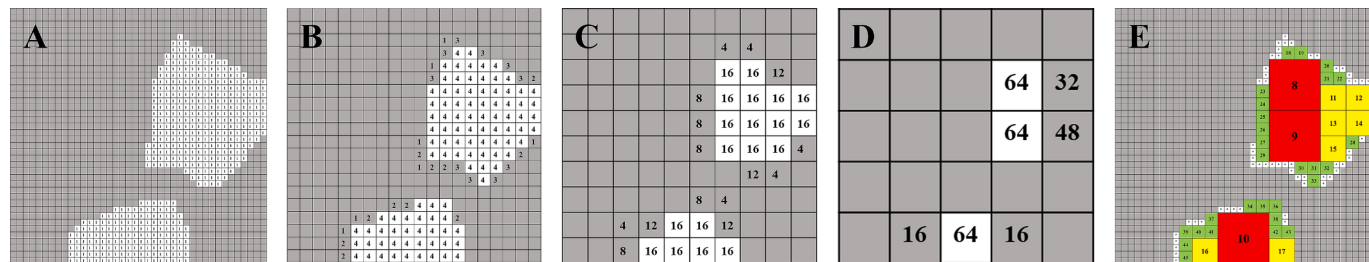


Fig. 3. Schematic of the basic coarsening algorithm. (A) The binary image in which the white denotes the microporosity, and the grey denotes macropores and solid. (B) The feature map with their cell values after the first convolution operation. (C) The feature map with their cell values after the second convolution operation. (D) The feature map with their cell values after the third convolution operation. (E) The computational grids of the microporosity where the red, the yellow, and the green respectively denote the third-level coarsening grids with the size of 4^3 pixels, the second-level coarsening grids with the size of 4^2 pixels, and the first-level coarsening grids with the size of 4^1 pixels. The white denotes the uncoarsened grids (i.e., the same as the original microporosity voxels). (For interpretation of the references to color in this figure legend, the reader is referred to the web version of this article.)

different levels of coarsened grids. At the beginning of each convolution operation in the basic coarsening algorithm, we conduct erosion operation (from scikit-image in Python) on the filtered feature map (refer to Fig. 2), to find the outmost layer of the cells which satisfy the coarsening criterion. Notice that in the filtered feature map, the cells with non-zero values satisfy the coarsening criterion. Then, we reset the weight values in the cells belonging to the outmost layer to 0. In other words, we

prevent these cells in the feature map from participating in the next level of coarsening. Fig. 4A shows the computational grids of the microporosity under the transition-layer module. Compared to the grids in Fig. 3E, the stiffness of transition regions has been dramatically reduced, which is beneficial to the modeling of flow and transport in microporosity. We also observe that the third-level coarsening of this example is not achieved under the transition-layer module, because a number of

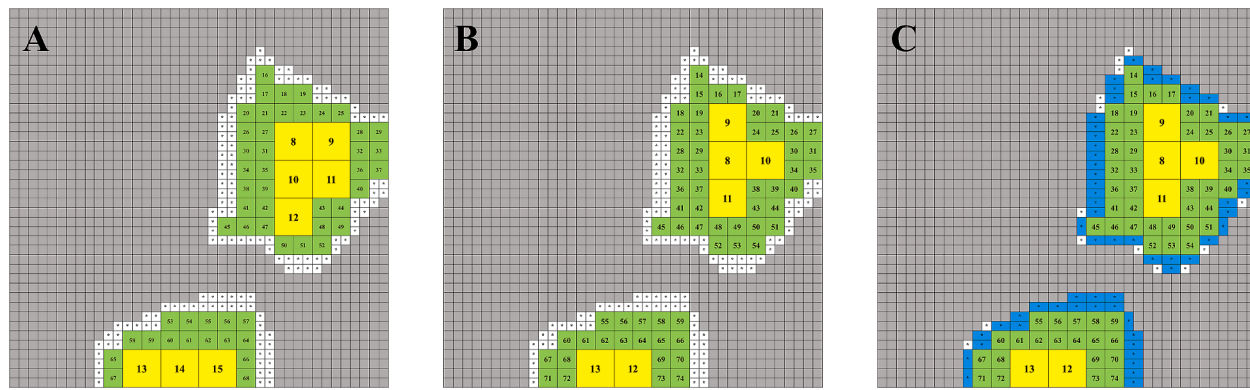


Fig. 4. Computational grids of the microporosity under different combinations of the three submodules. (A) Transition-layer module. (B) The combination of transition-layer module and outward-coarsening module. (C) The combination of transition-layer module, outward-coarsening module, and interface-coarsening module.

grids have been used as the transition layers.

The outward-coarsening module aims, in the last level of coarsening, to coarsen microporosity voxels by starting from the center of each microporosity region. As a result, the largest computational grids will always locate around the center of microporosity where flow gradients are usually lowest. To this aim, in the last convolution operation in the basic coarsening algorithm, we keep the kernel size but change the stride to 1. The resultant feature map will be the same size as the previous level feature map. Then, the Euclidean distance map of the feature map is calculated, while the cells with a weight value of 0 are set to solid.

Once the Euclidean distance map is available, we can start the coarsening and numbering with the cell of the largest distance in each microporosity region, and repeat searching neighboring cells till no more voxels can be coarsened. Finally, the computational grids of the microporosity under the combination of transition-layer module and outward-coarsening module are shown in Fig. 4B. It can be seen that the second-level coarsening grids will locate in the center of each microporosity region, and the numbering of the computational grids is outward.

As shown in Fig. 4A and 4B, the majority of the computational grids, as the microporosity voxels, locate in the vicinity of void-microporosity and solid-microporosity interfaces. To reduce the number of these grids,

we develop the interface-coarsening module. In addition to the kernel used in the basic coarsening algorithm, we design three more kernels with the sizes of $2 \times 2 \times 1$, $2 \times 1 \times 2$, and $1 \times 2 \times 2$ along the x, y, and z directions, respectively. Meanwhile, the corresponding strips are the same size as the kernels. After the basic coarsening algorithm is finished, for the input binary image, we reset the weight values of the interface voxels to 1 and the remainder to 0. Through three independent convolution operations with the above three kernels, like in the basic algorithm, we can coarsen and number the interface voxels. Fig. 4C shows the computational grids of the microporosity under the combination of transition-layer module, outward-coarsening module, and interface-coarsening module. Notice that in 2D the used kernels are 2×1 and 1×2 along the x and y direction, respectively. It is seen that most of the interface voxels are coarsened into the grids with the size of 2×1 voxels, because the convolution operation with the kernel of 2×1 is first conducted.

2.3. Fusion of the pore network and microporosity grids

To get the computation mesh for a hybrid model solver, the final step is to fuse the pore network of macropores and the computational grids of microporosity. As described in Section 2.1 and 2.2, a rigorous

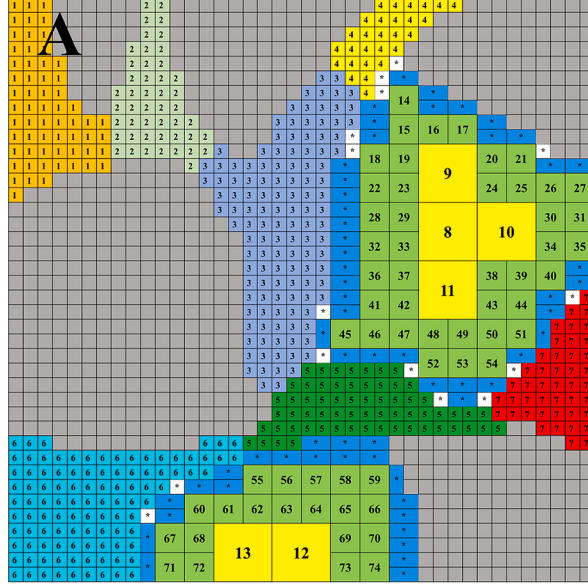


Fig. 5. Schematic of the fusion of the pore network of macropores and the computational grids of microporosity. (A) Watersheds voxels, microporosity grids, and their connections. (B) The final computational mesh which composes the pore network and the microporosity grids.

numbering system for both pore network and microporosity grids has been employed. As shown in Fig. 5, the pore bodies and their associated watershed voxels are numbered in the same way. On the other hand, in the basic coarsening algorithm and the three submodules, each computational grid of microporosity and its associated microporosity voxels are always linked, and numbered in the same way. Moreover, we first number pore bodies of the pore network, then the computational grids of microporosity. So, once the pore-network extraction and the coarsening of microporosity voxels are done, we can loop through all the numbered voxels, and obtain the connectivity map between pore bodies and microporosity grids.

We end up with a brief introduction to the data structure used in computational meshes. Basically, the data of a computational mesh are stored in two files. One file is used to store the information on pore bodies and microporosity grids, which includes centroid, volume, inscribed radius, and surface area of each pore body, and centroid, porosity, dimensions of each microporosity grid. The other file is used to store the information on pore throats and faces of microporosity grids, which includes the numbers of the two connected pore bodies, inscribed radius, area, perimeter, and length of each pore throat, and the numbers of the two connected grids (or a pair of pore body and grid), centroid, dimensions, unit normal of each grid face.

For pore throats, we store inscribed radius, area, and perimeter. For microporosity grids, we store the center location, length-width-height, and volume. In the connectivity map, we store the face center, normal, face dimensions, and area. This information is needed in the physical models.

3. Physical models and their numerical implementation

To thoroughly investigate the impact of grid coarsening in microporosity on the numerical modeling of flow and transport, in this work, we implement three physical models (Zhang et al., 2019), namely, incompressible single-phase flow, transient compressible single-phase flow, and transient solute transport. Moreover, we consider isothermal cases.

3.1. Incompressible single-phase flow

We consider an incompressible single-phase flow in multiscale digital rocks. In the framework of a pore-network-continuum hybrid model, the flow in macropores is discretized by a pore-network model as:

$$\sum_{j=1}^{N_i} T_{ij} (p_i - p_j) = 0 \quad (1)$$

where i is the pore body index, j is the index of neighboring pore body or microporosity grid, N_i is the full coordination number of pore body i , p is the pressure, T_{ij} is the transmissibility, and we neglect the gravitational force. For a pair of pore bodies, we assume all the viscous resistances are lumped into the pore throat; then, T_{ij} is given by:

$$T_{ij} = \frac{\pi R_{ij}^4}{8\mu l_{ij}} \quad (2)$$

where R_{ij} is the equivalent radius of pore throat ij with respect to the pore-throat cross-sectional area, l_{ij} is the pore-throat length, μ is the dynamic viscosity.

The flow in microporosity is assumed to be described by the Darcy's law, resulting in the following conservation equation:

$$\nabla \bullet \mathbf{q} = \nabla \bullet \left(-\frac{k}{\mu} \nabla p \right) = 0 \quad (3)$$

where \mathbf{q} is the Darcy velocity. The control volume method is used in microporosity, associated with a Two-Point Flux Approximation (TPFA) scheme (Karimi-Fard et al., 2004; Aarnes et al., 2007). This gives rise to

a similar form of discretized conservation equation as equation (1). Moreover, as illustrated in Fig. 6b, for a pair of microporosity grids, T_{ij} is given by the harmonic average of the two transmissibilities:

$$T_{ij} = \frac{a_i a_j}{a_i + a_j} \text{ with } a_i = \frac{A_i k_i}{\mu d_i} \mathbf{n}_i \bullet \mathbf{f}_i, a_j = \frac{A_j k_j}{\mu d_j} \mathbf{n}_j \bullet \mathbf{f}_j \quad (4)$$

where a_i is the transmissibility of grid i (or CV_i), a_j is the transmissibility of grid j , A_i is the interface area between two control volumes, k_i is the intrinsic permeability of grid i , d_i is the distance between the centroid of the interface and the centroid of grid i , \mathbf{n}_i is the unit vector normal to the interface inside grid i , and \mathbf{f}_i is the unit vector along the direction of the line joining the centroid of grid i to the centroid of the interface.

At the interfaces of macropores and microporosity, we impose the conditions of flux and pressure continuities. As illustrated in Fig. 6C, for a pair of pore body and microporosity grid, T_{ij} is given by the harmonic average of the two transmissibilities as (Karimi-Fard et al., 2004):

$$T_{ij} = \frac{a_i a_j}{a_i + a_j} \text{ with } a_i = \frac{\pi R_i^4}{8\mu l_i}, a_j = \frac{A_j k_j}{\mu d_j} \mathbf{n}_j \bullet \mathbf{f}_j \quad (5)$$

where a_i is the transmissibility of pore body i , a_j is the transmissibility of microporosity grid j , R_i is the equivalent radius with respect to the pore-body volume, l_i is the half pore-body length assumed to be equal to R_i , A_j is the interface area between pore body and microporosity grid, k_j is the intrinsic permeability of grid j , and d_j is the distance between the centroid of the interface and the centroid of grid j , \mathbf{n}_j is the unit vector normal to the interface inside grid j , and \mathbf{f}_j is the unit vector along the direction of the line joining the centroid of grid j to the centroid of the interface.

Finally, all the discretized conservation equations can be assembled, yielding a coupled global system for solving pressure:

$$\begin{bmatrix} \text{PNM transmissibility} & \text{coupling of PNM and Darcy} \\ \text{coupling of Darcy and PNM} & \text{Darcy transmissibility} \end{bmatrix} \begin{bmatrix} p_{\text{PNM}} \\ p_{\text{Darcy}} \end{bmatrix} = [b] \quad (6)$$

3.2. Transient compressible single-phase flow

In the second physical model, we consider a transient compressible single-phase flow in multiscale digital rocks, to simulate gas production. The flow in macropores is discretized by a pore-network model and the backward Euler method as:

$$V_i \frac{p_i^{t+\Delta t} - p_i^t}{\Delta t} = - \sum_{j=1}^{N_i} \rho_i^{t+\Delta t} \max(Q_{ij}^{t+\Delta t}, 0) - \sum_{j=1}^{N_i} \rho_j^{t+\Delta t} \min(Q_{ij}^{t+\Delta t}, 0) \quad (7)$$

where V_i is the volume of pore body i , ρ is the gas density, Q_{ij} is the volumetric flow rate given by the Hagen-Poiseuille equation as $Q_{ij} = T_{ij}(p_i - p_j)$, t is the current time, and Δt is the time step. We use the upwind gas density to calculate mass flow rates inward and outward the pore body. Without loss of generality, we assume the idealized gas law which relates density to pressure as $p = \rho RT$ where R is the universal gas constant and T is the temperature. Then, equation (7) can be cast into:

$$V_i \frac{p_i^{t+\Delta t} - p_i^t}{\Delta t} = - \sum_{j=1}^{N_i} p_i^{t+\Delta t} \max(T_{ij}(p_i^{t+\Delta t} - p_j^{t+\Delta t}), 0) - \sum_{j=1}^{N_i} p_j^{t+\Delta t} \min(T_{ij}(p_i^{t+\Delta t} - p_j^{t+\Delta t}), 0) \quad (8)$$

where gas pressure at the new time is the only unknown variable, and the transmissibility is the same as in equation (2).

With the assumption of idealized gas law, the mass conservation in microporosity is given as:

$$\frac{\varepsilon}{RT} \frac{\partial p}{\partial t} + \nabla \bullet \left(-\rho \frac{k}{\mu} \nabla p \right) = 0 \quad (9)$$

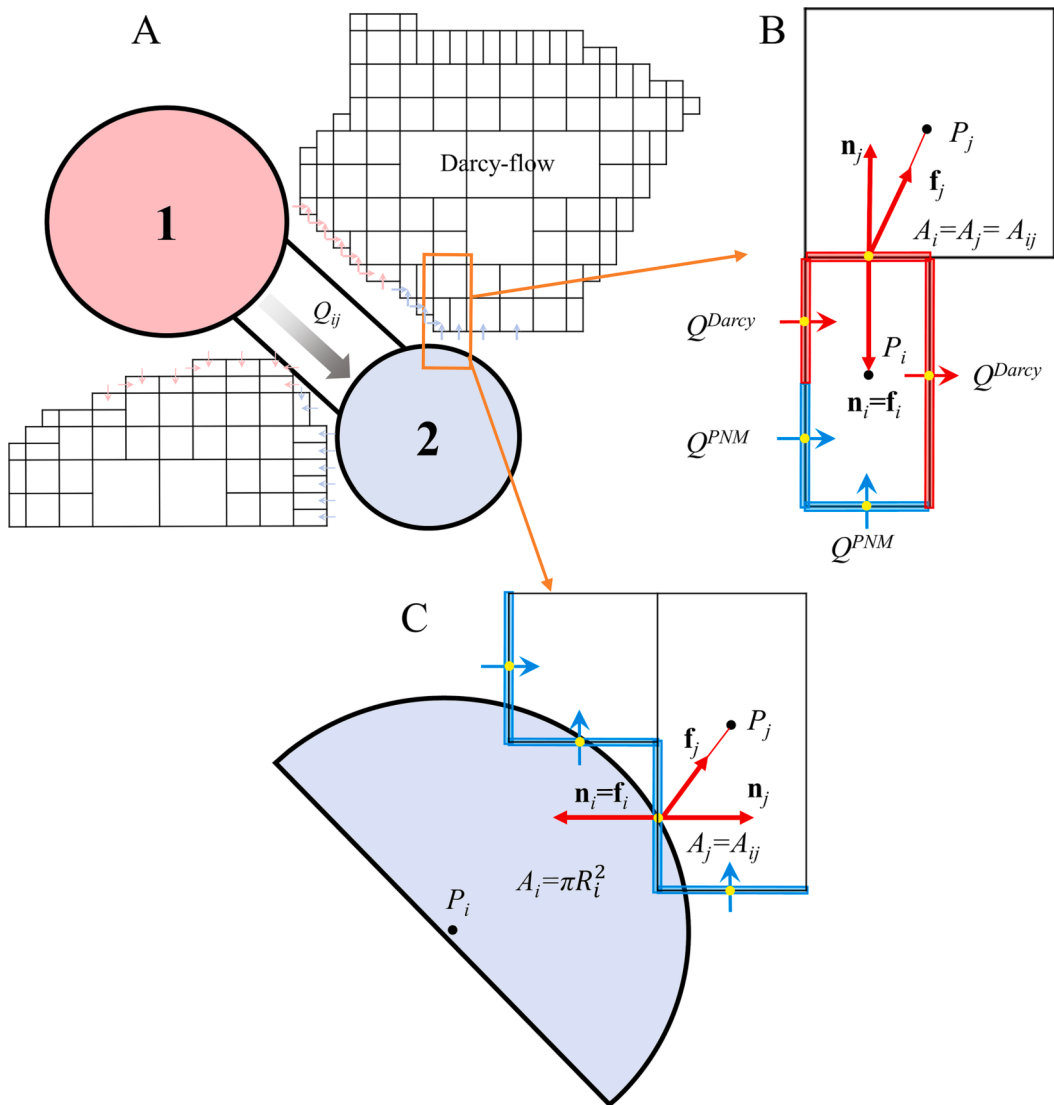


Fig. 6. (A) Schematic of the interface coupling between macropores and microporosity. (B) Geometrical representation of two adjacent control volumes and the definition of different parameters involved in transmissibilities in microporosity. (C) Geometrical representation between a macropore and microporosity.

where ε is the porosity. We use the finite volume method and the backward Euler method to discretize the equation. The interface condition and treatment are the same as those in equation (5). Moreover, it is worth noting that the unknown variable $p^{t+\Delta t}$ will go into the coefficient matrix (refer to equation (6)), yielding a nonlinear system of algebraic equations for solving pressure.

3.3. Transient solute transport

In the last physical model, we consider passive transport of a dilute solute in water. We neglect dispersion in both macropores and microporosity, due to small Péclet number values under consideration. In the modeling, incompressible water flow is solved by the model presented in Section 3.1, which provides the flux field to solute transport. Solute transport in macropores is discretized by a pore-network model and the backward Euler method as:

$$V_i \frac{C_i^{t+\Delta t} - C_i^t}{\Delta t} = - \sum_{j=1}^{N_i} C_i^{t+\Delta t} \max(Q_{ij}, 0) - \sum_{j=1}^{N_i} C_j^{t+\Delta t} \min(Q_{ij}, 0) - \sum_{j=1}^{N_i} \Gamma_{ij} (C_i^{t+\Delta t} - C_j^{t+\Delta t}) \quad (10)$$

where C_i is the solute molar concentration in pore body i , Q_{ij} is the flux

from the steady-state single-phase flow simulation, Γ_{ij} denotes the diffusive transmissibility for solute diffusion. For a pair of pore bodies, Γ_{ij} is approximated by:

$$\Gamma_{ij} = \frac{A_{ij} D_{ij}}{l_{ij}} \quad (11)$$

where A_{ij} is the cross-sectional area of pore throat ij , D_{ij} is the molecular diffusivity.

The mass conservation of solute in microporosity is given as:

$$\varepsilon \frac{\partial C}{\partial t} + \mathbf{q} \bullet \nabla C - \nabla \bullet (D \nabla C) = 0 \quad (13)$$

which is discretized by the finite volume method and the backward Euler method. For a pair of microporosity grids, Γ_{ij} is given by the harmonic average of the two diffusive transmissibilities:

$$\Gamma_{ij} = \frac{a_i a_j}{a_i + a_j} \text{ with } a_i = \frac{A_i D_i^\varepsilon}{d_i} \mathbf{n}_i \bullet \mathbf{f}_i, a_j = \frac{A_j D_j^\varepsilon}{d_j} \mathbf{n}_j \bullet \mathbf{f}_j \quad (14)$$

where D_i^ε is the effective molecular diffusivity in microporosity grid i . The resultant discretized equation is similar to equation (10) where V_i is replaced with $V_i \varepsilon_i$.

At the interfaces of macropores and microporosity, we impose the conditions of solute flux (both advective and diffusive ones) and concentration continuities. For a pair of pore body and microporosity grid, similar to the calculation of T_{ij} in equation (5), Γ_{ij} is given by:

$$\Gamma_{ij} = \left(\frac{A_i D_i}{l_i} \frac{A_j D_j^e \mathbf{n}_j \bullet \mathbf{f}_j}{d_j} \right) / \left(\frac{A_i D_i}{l_i} + \frac{A_j D_j^e}{d_j} \mathbf{n}_j \bullet \mathbf{f}_j \right) \quad (15)$$

where A_i is the equivalent cross-sectional area as πR_i^2 , D_i is the molecular diffusivity, and D_j^e is the effective diffusivity in microporosity grid j . Notice that D_i is equal to D_{ij} in equation (11) so long as dispersion in macropores is negligible. Finally, notice that the advective flux Q_{ij} will go into the coefficient matrix (refer to equation (6)), yielding a linear system of algebraic equations for solving concentration.

4. Results and discussion

Two multiscale digital rocks with different complexities of porous structures have been used in this work, namely, a synthesized multiscale Berea sandstone and a real Estaillades carbonate rock. Their numerical results of flow and transport are presented separately.

4.1. Synthesized multiscale digital rock

4.1.1. Computational meshes

A digital rock of Berea sandstone from the Imperial College Open Source library is used. It has the size of 400^3 voxels with the resolution of $5.345\text{ }\mu\text{m}$. To reduce computational efforts, we extracted a 200^3 sub-volume from the image as our study domain. As shown in Fig. 7A, the white and blue voxels are solid and void spaces, respectively. The porosity and permeability of the subvolume are 19.8 % and 0.8 Darcy, respectively, which are close to those (19.6 % and 1.2 Darcy) of the original image. To synthesize a multiscale digital rock, we first generated the watersheds of solid and void spaces, and then randomly filled 25 % of solid watersheds and 25 % of void watersheds by microporosity, corresponding to a ratio of grain-filling to pore-filling of 1. The final ternary image is shown in Fig. 7B, where the blue and grey are macropores and microporosity, respectively. The numbers of their voxels are around 1.22 million and 1.9 million respectively. For simplicity, microporosity here is assumed to be homogeneous and isotropic with porosity of 31 %. The total porosity of the whole multiscale digital rock is around 22 %.

With a maximum of three-level coarsening, three types of microporosity grids were generated by the developed algorithm in Section 2, which were labeled as CG1, CG2, and CG3. CG0 consisting of original microporosity voxels was set as the reference to evaluate the performance of CG1, CG2, and CG3. CG1 was generated by the basic coarsening algorithm with a kernel size of 2^3 . CG2 has the highest mesh quality, which was generated by the basic coarsening algorithm together

with the transition-layer module and the outward-coarsening module. CG3 was generated by the basic coarsening algorithm together with the transition-layer module, the outward-coarsening module, and the interface-coarsening module as shown in Fig. 7C. Moreover, to further reduce the number of grids in the vicinity of the interfaces between macropores and microporosity, we deactivate erosion operation in the first level coarsening. In other words, the maximum grid size on the interfaces is 2^3 voxels as shown in Fig. 7D. Therefore, GC3 should have higher mesh quality than GC1. Table 1 gives the details of the four computational meshes, which will be used in the modeling of flow and transport.

4.1.2. Absolute permeability

For an incompressible single-phase flow, we impose the inlet and outlet pressure boundary conditions along the Z direction and the no-flux boundary condition for the remainder. The pressure difference between the inlet and outlet is set to 100 Pa. Notice that the inlet and outlet can include both macropores and microporosity grids, depending on the porous structures under study. The resultant system of linear algebraic equations for pressures in both macropores and microporosity are solved by the open source library, Eigen (Guennebaud G, Jacob B, et al., 2010). Three microporosity permeabilities of 5 mD, 50 mD, and 500 mD have been used in the simulations, and the corresponding absolute permeabilities of the multiscale rock are calculated by the Darcy equation. With CG0 microporosity grids, the absolute permeabilities of 229 mD, 297 mD, and 737 mD for the artificial sample are obtained for microporosity permeabilities of 5 mD, 50 mD, and 500 mD, respectively. Because half of the microporosity in the synthesized multiscale rock is the pore-filling type, the absolute permeabilities are smaller than that (i.e., 800 mD) of the original Berea rock.

To evaluate the impact of coarsening microporosity on the prediction of permeability, we calculate the relative errors (%) for microporosity grids CG i ($i = 1, 2, 3$) by $RE_{CGi}\text{ }(\%) = 100 \times (K_{CG0} - K_{CGi}) / (K_{CG0} - K_{PNM})$, where K_{PNM} is the permeability (219 mD) of the pore-network of macropores. As shown in Fig. 8, the absolute

Table 1
The details of CG0, CG1, CG2, and CG3 microporosity grids.

Grid type	CG0	CG1	CG2	CG3
macropores	468			
$8 \times 8 \times 8$	–	1003	40	98
$4 \times 4 \times 4$	–	9520	8350	10,377
$2 \times 2 \times 2$	–	60,341	93,009	111,405
$2 \times 2 \times 1$	–	–	–	24,945
$2 \times 1 \times 2$	–	–	–	10,964
$1 \times 2 \times 2$	–	–	–	6242
$1 \times 1 \times 1$	1,901,511	295,967	602,559	127,363
In total	1,901,979	367,299	704,426	291,862
Reduction of grids	0 %	80.7 %	63 %	84.7 %

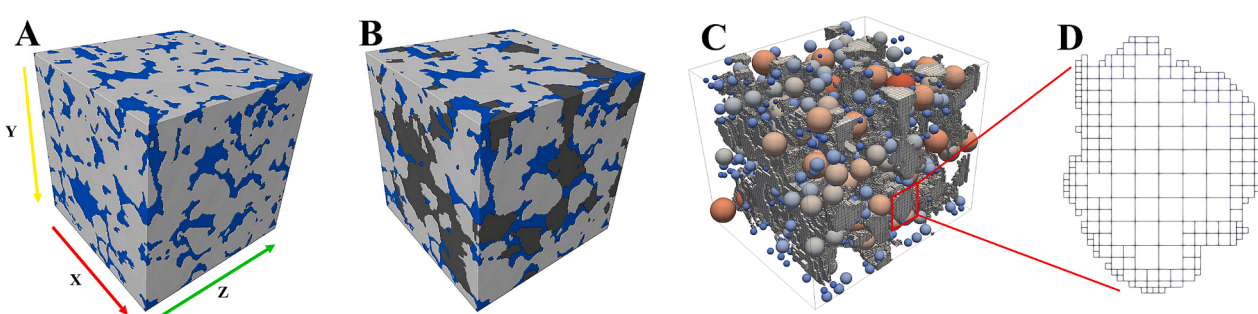


Fig. 7. (A) 3D binary image of Berea sandstone (200^3 voxels) in which the white represents non-porous solid, and the blue represents void spaces. (B) The synthesized multiscale Berea digital rock in which 25% of solid and 25% of void spaces are filled with microporosity in grey color. (C) The computational mesh with CG3 coarsened microporosity grids. (D) A 2D zoom-in of microporosity grids. (For interpretation of the references to color in this figure legend, the reader is referred to the web version of this article.)

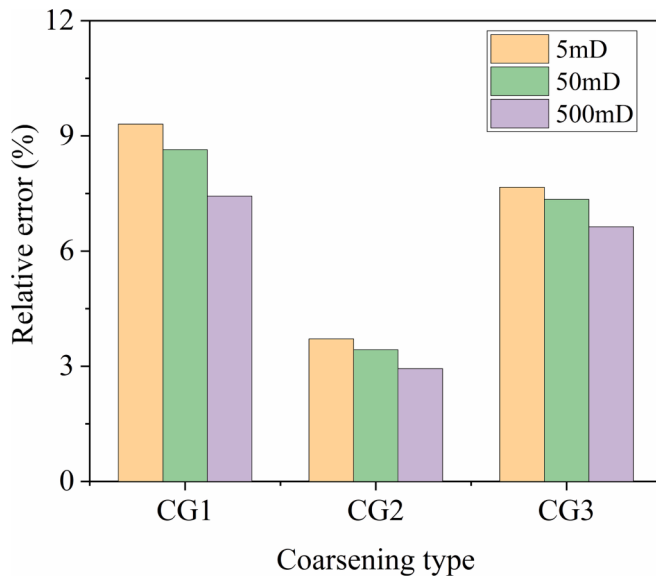


Fig. 8. Impact of coarsening microporosity on the prediction of absolute permeability.

permeabilities of the multiscale rock under different microporosity permeabilities are underestimated. CG2, with the highest mesh quality, gives rise to the smallest relative errors of around 3 %. However, it needs the most computational efforts (see Fig. 12A). Compared to CG2, CG3 doubles the relative errors. This indicates that high-resolution interface grids between macropores and microporosity are beneficial to numerical accuracy. Moreover, if only the basic coarsening algorithm is used as for CG1, the largest relative errors are seen.

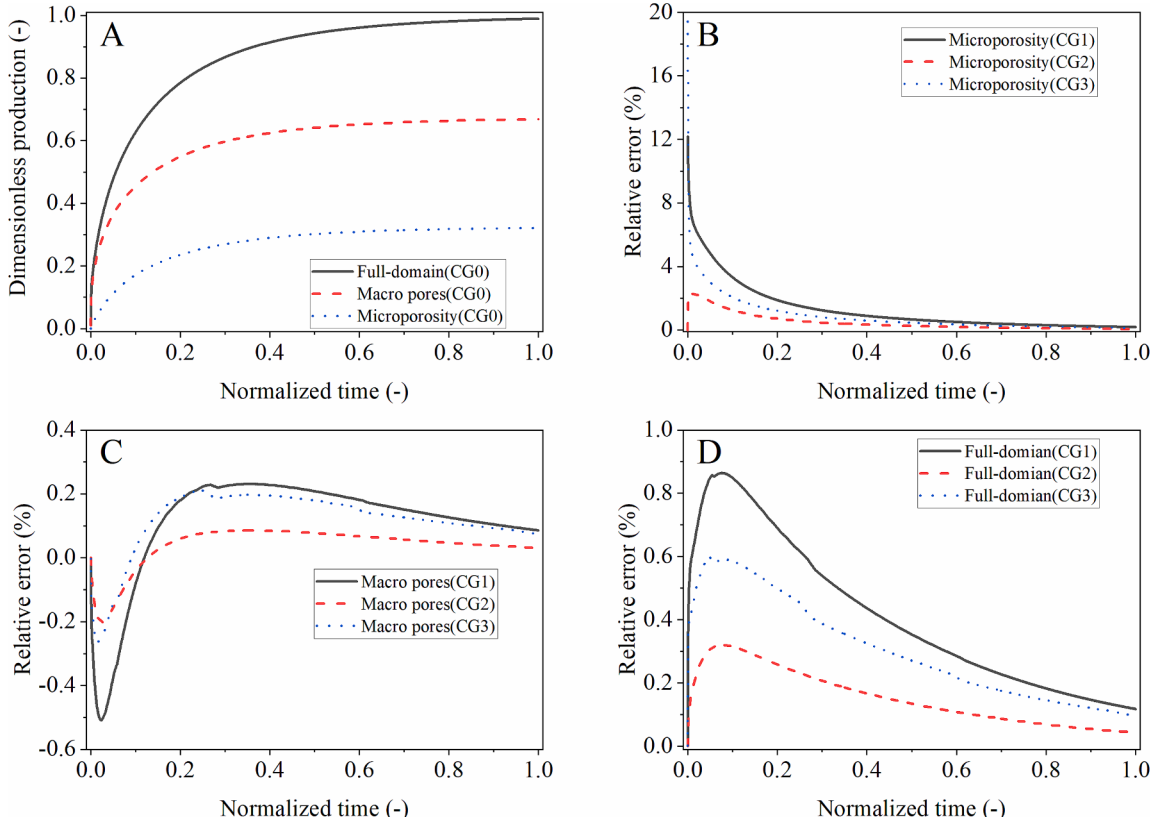


Fig. 9. (A) The dimensionless gas production over time from microporosity, macropores, and full-domain of CG0. (B-D) The relative errors of gas production for the three coarsening schemes compared with the reference value (i.e., gas production of CG0).

schemes underestimate the gas production of microporosity, because coarsening deteriorates the accuracy of pressure gradients in microporosity. It is seen that CG2 presents the smallest relative errors followed by CG3 and CG1. Moreover, as expected, they are profound at the early stage of gas production, where pressure gradients are large. Due to the complex flow interactions between microporosity and macropores, coarsening also leads to the errors in macropores, but they are significantly smaller than those of microporosity as shown in Fig. 9C. Finally, the relative errors of the total gas production are shown in Fig. 9D. For the case studies in this work, CG2 results in the smallest errors followed by CG3 and CG1, which are consistent with the permeability simulations in Section 4.1.2.

4.1.4. Transient solute transport

In the case studies of transient solute transport, a steady-state flow field is first built, where the pressure drop along the Z direction is set to 100 Pa. Instead of the water flow rate, we vary the molecular diffusivity of solute, to obtain different Péclet number values (i.e., $Pe = qL/D$ where q is the Darcy velocity, L is the domain length, and D is the molecular diffusivity). For each mesh type, case studies under four different Pe values (i.e., 0.1, 1, 10, 100) are conducted. For the solute transport equations (11), (14), we impose the inlet concentration of 1 mol/m³ at the min Z, and the Neumann boundary condition of zero concentration gradient at the max Z. Solute is initially absent in the domain. The time step is determined by $\Delta t = \min(V_i \varepsilon_i / Q_i^{out}, l_i^2 / 4D_{ij})$, where Q_i^{out} is the fluid outflux in either pore body i or microporosity grid i (Qin et al., 2016). Finally, for all the simulations, we set the porosity, permeability, and effective diffusivity coefficient of solute to 0.31, 5 mD, and 0.09, respectively. For comparisons among different numerical results, each numerical simulation is ceased when the outlet solute concentration reaches 99 % of the inlet concentration.

To make numerical results more intuitive, we use the inlet concentration to define the dimensionless average outlet concentration, and the transport time of each case is also nondimensionalized by a fixed advection time, $t = L/v$, where v is the Darcy velocity. Fig. 10 shows the

concentration distributions in CG0 under different Pe values. With the increase of Pe , the migration modal of solute changes from diffusion to advection. Microporosity generally retards solute transport due to its much lower transmissibility. If we treat microporosity as solid phase in the image segmentation, as shown in Fig. 11A, the breakthrough curve would be steeper under $Pe = 100$, while the effect of microporosity on the breakthrough curve is minor under $Pe = 0.1$ as expected. Fig. 11B shows the breakthrough curves of CG0 under four different Pe values. It can be seen that the larger the Pe value is, the longer the tailing of the breakthrough curve is. Notice that in our case studies we decrease solute diffusivity to obtain a larger Pe value. Therefore, increasing Pe causes less solute transport from macropores to microporosity, and then longer tailing of the breakthrough curve. Moreover, it is found that the breakthrough curves intersect each other. This phenomenon can be well explained as follows. Under a large Pe value (e.g., 100 in our case studies), solute prefers to transport in connected macropores by advection, and slowly diffuses into microporosity (refer to Fig. 10); as a result, we would expect a high outlet concentration early and a long tailing of the breakthrough curve. In the opposite, under a smaller Pe value (e.g., 1.0), both advection and diffusion are important to solute transport; as a result, we would expect high outlet concentration later, and the breakthrough curve will intersect with that of a large Pe value as shown in Fig. 11B.

We take the breakthrough curve of CG0 as the reference to calculate the relative errors for the three different coarsening schemes by $RE_{CGi} (\%) = 100 \times (C_{CG0} - C_{CGi})/C_{CG0}$. Because the trends of relative errors under Pe values of 1, 10, and 100 are similar, we only plot the results of $Pe = 0.1$ and $Pe = 100$ in Fig. 11C and Fig. 11D, respectively. It is seen that the absolute relative errors decrease over time for each type of mesh. Under high Pe values, the relative errors are minor but negative, which means coarsening microporosity slightly overestimates the breakthrough curve. While under low Pe values, the relative errors are large (up to 10 % at the beginning) and positive, which means coarsening microporosity underestimates the breakthrough curve. As we know, under high Pe values, microporosity retards solute transport, and

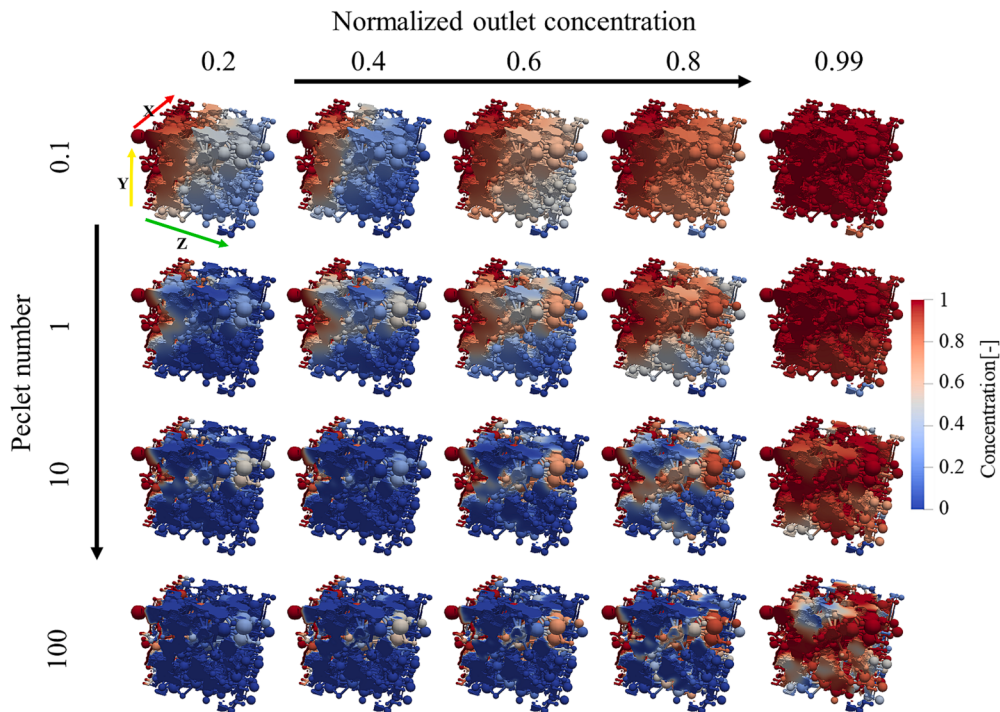


Fig. 10. Distributions of solute concentration normalized by the inlet concentration in CG0 under different Péclet number values, and normalized outlet concentration values. From top to bottom, the Péclet number value increases from 0.1 to 100. From left to right, the normalized outlet concentration increases from 0.2 to 0.99.

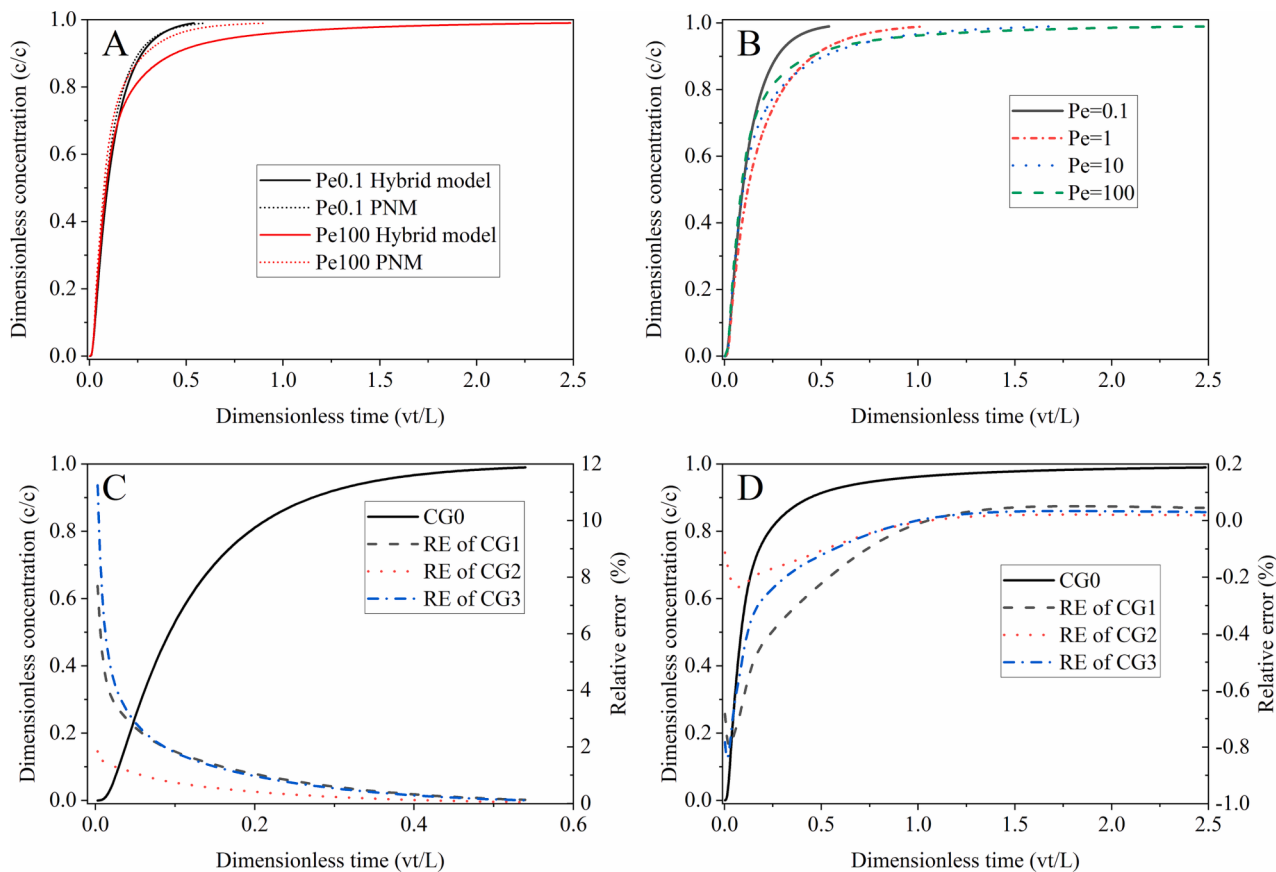


Fig. 11. (A) The breakthrough curves of CG0 under four different Pe values. The horizontal axis denotes the dimensionless transport time normalized by the advection time. The vertical axis denotes the dimensionless averaged outlet concentration normalized by the inlet concentration. (B) The breakthrough curves of CG0 under $Pe = 0.1$ and $Pe = 100$, with and without the involvement of microporosity. In the latter case, we only simulate solute transport in macropores while microporosity is assumed to be solid. (C) and (D) The relative errors of the breakthrough curves from the three coarsened meshes compared with CG0 under $Pe = 0.1$ and $Pe = 100$.

coarsening microporosity would underestimate solute transport from macropores to microporosity. As a result, the breakthrough curve will be overestimated and the relative errors will be negative.

4.1.5. Reduction of computation

The computational cost is an important metric to evaluate the performance of coarsening microporosity. In this work, all the simulations are performed by using a single core on a personal computer with an i7-10700 CPU. The adapting time steps and residuals for convergence (10^{-8}) are identical for the different coarsening schemes. The speedup ratio is the ratio of the computation time of CG0 to that of CGi. Either a compressible flow or solute transport simulation of CG0 needs several weeks to accomplish. As shown in Fig. 12, for different case studies, the speedup ratios are $0.9 \sim 2$ times the coarsening ratios (see Table 1).

In the permeability modeling, as shown in Fig. 12A, the increase of

microporosity permeability leads to faster convergence. The maximum speedup ratio of CG3 can reach 12. For the compressible gas production simulations with the microporosity permeability of 5 mD, similar to the permeability modeling, the speedup ratios are approximately equal to the coarsening ratios. For the solute transport simulations, the speedup ratio can be increased at low Pe values. Overall, coarsening microporosity substantially reduces computation time and memory required for matrix assembly and numerical iterations. Based on the case studies in this work, the coarsening scheme of CG3 is regarded to be optimal, which can balance accuracy and computational efficiency. Finally, it is worth noting that the speedup ratios can be substantially increased by optimizing the numerical implementational algorithms, which is beyond the scope of this work.

4.2. Estaillades carbonate rock

The second test sample is an Estaillades carbonate rock, which is composed of 99 % calcite and contains both intergranular macropores and sub-resolution intragranular microporosity (Dautriat et al., 2011). The raw data, including the CT images of dry, saturated, and different capillary pressures, as well as the porosity map, and the invasion capillary pressure (denoted by P_{ct}) map, were published by (Wang et al., 2022) on the Digital Rock Portal (<https://www.digitalrockspotal.org/projects/363>). The porosity map was acquired by comparing the differences between the scanning images taken under dry and saturated conditions. The CT images under different capillary pressures were processed by the differential imaging technology to obtain the P_{ct} map. The introduced data is very suitable to test and study our hybrid model.

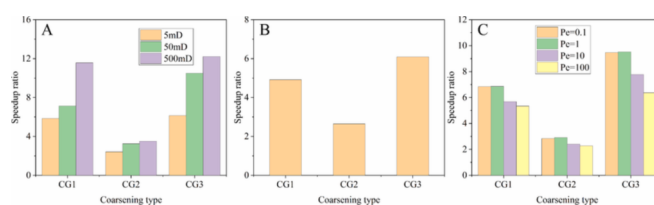


Fig. 12. Speedup ratios by coarsening microporosity under different modeling scenarios: (A) permeability simulations, (B) compressible gas production simulations with the microporosity permeability of 5 mD, and (C) solute transport simulations.

To reduce computational efforts, we extract a subdomain of 400^3 voxels from the original images ($1316 \times 1316 \times 1087$ voxels with the voxel resolution of $6.5 \mu\text{m}$). The macropores and microporosity of the subdomain account for 6 % and 64.8 % of the whole voxels, respectively. The total porosity is 24.2 %, which is basically consistent with the value of the original image (25.4 %). We adopt the optimal coarsening scheme of CG3 discussed in Section 4.1 to generate the computational mesh, which contains 1817 macropores and about 4.34 million microporosity grids as shown in Fig. 13A. The number of computational grids is reduced by about 90 % compared to the number of original microporosity voxels. Moreover, the porosity and invasion capillary pressures of microporosity grids are obtained by averaging the corresponding voxel values of each grid based on the original porosity and P_{ct} maps. Fig. 13B and Fig. 13C show the distributions of P_{ct} and porosity in the coarsened microporosity grids.

In practice, according to the characterization level of porous structures of a multiscale digital rock, we may model its permeability in two ways. In the first case study, we have the data of porosity and invasion capillary pressure maps. Then, the absolute permeability of each microporosity grid may be estimated by the Katz-Thompson equation (Katz & Thompson, 1986), $k = \varepsilon r^2 / 32\tau^2$, where ε is the porosity, τ is the tortuosity, and r is the mean pore radius. Furthermore, we assume the same type of microporosity with a constant tortuosity of 1.75. The mean pore size is calculated by the Young-Laplace equation, $r = 2\sigma\cos\theta/P_c$, where P_c is approximated by P_{ct} , σ is the water-decane interfacial tension of 48.3 mN/m , and θ is the static contact angle which is assumed to 0° (Wang et al., 2022).

Experimentally determining the P_{ct} map is usually costly and time-consuming. Moreover, it has been shown that mean pore sizes (or P_{ct}) are not correlated to microporosity porosity for Estaillades (Wang et al., 2022). Therefore, in case 2, we may assume a unified average pore radius for all microporosity, which can be calculated from a capillary pressure curve. Here, we use the capillary pressure curve of the Estaillades core given by (Bultreys et al., 2015), and the computed average pore radius is $3.6 \mu\text{m}$. Together with the porosity map, we can use the Katz-Thompson equation to estimate the absolute permeability of each microporosity grid.

The predicted permeability of case 1 is 160.1 mD , which is in good agreement with the reported values of $86.4 \sim 326.0 \text{ mD}$ (Bauer et al., 2012; Blunt et al., 2013; Alyafei & Blunt, 2016). To some extent, this indicates the reliability of our hybrid model for a realistic multiscale digital rock. In comparison to case 1, a much lower permeability of 41.8 mD is predicted in case 2. This illustrates on the important role of pore-size heterogeneity of microporosity in the permeability modeling, and it would also apply to other flow and transport processes. To further highlight the importance of characterizing the pore-size heterogeneity of microporosity, Fig. 14 shows the pressure distributions in the two case studies and their pressure difference. It is seen that the maximum pressure difference is up to $\pm 15 \%$ concerning the pressure drop throughout the domain.

5. Conclusions and outlook

Multiscale porous structures in many geological rocks pose great challenges for digital rock physics in both imaging and modeling aspects. A pore-network-continuum hybrid modeling framework is promising to numerical studies of flow and transport in a standard multiscale digital rock, but remains computationally expensive. In this work, we have developed a novel and robust algorithm for coarsening microporosity voxels of a multiscale digital rock, which includes a basic coarsening scheme and three additional modules with various enhancements. Together with the pore network of macropores by image-based extraction, we can generate efficient computational meshes for hybrid modeling. Moreover, we have numerically implemented the hybrid models of single-phase incompressible flow, transient compressible flow, and transient solute transport. A number of case studies of synthesized multiscale digital rocks and natural Estaillades rock have been conducted, mainly to investigate the performance of the developed microporosity coarsening algorithm and the effects of microporosity on flow and transport in multiscale rocks. The main conclusions drawn from our studies are:

- (1) For a multiscale digital rock with half pore-filling and half grain-filling homogeneous microporosity, a three-level coarsening of microporosity can be achieved, and reduces the computational mesh by more than 80 %. The coarsening has negligible impacts on compressible gas production curves and breakthrough curves of solute transport, and the relative errors of permeability prediction are below 10 %.
- (2) Pore-filling microporosity provides the connectivity of macropores, which contributes to the intrinsic permeability of a multiscale rock, particularly for highly permeable microporosity. Microporosity retards solute transport, and influences breakthrough curves considerably. It also significantly influences gas production curves. In practice, microporosity needs to be considered for the modeling of multiscale digital rocks.
- (3) The developed pore-network-continuum hybrid model is suitable to a realistic multiscale digital rock. It can substantially reduce computational efforts, while keeping the high resolution of microporosity heterogeneities. Fine characterization of pore-size distributions in microporosity is crucial to the prediction of rock permeability as well as local flow fields.

Finally, we comment on a few aspects regarding the present pore-network-continuum hybrid model aided by grid coarsening. First, compared to DPNMs, our model can capture microporosity heterogeneity at a higher spatial resolution, while maintaining much of the computational efficiency. However, parallel computing may need to be employed if additional complexities are considered, particularly for transient case studies and extended multiphase dynamics. Second, the current algorithm of microporosity coarsening uses a geometrically dependent criterion to determine which voxels to coarsen. This may lead

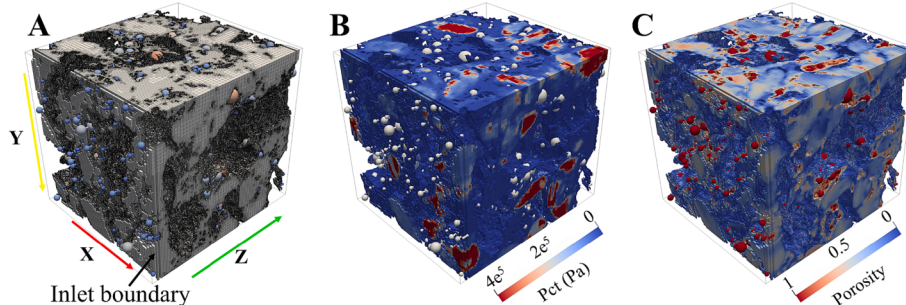


Fig. 13. (A) The computational grids by the optimal coarsening scheme of CG3. (B) The invasion capillary pressure and (C) porosity distributions of the computational grids.

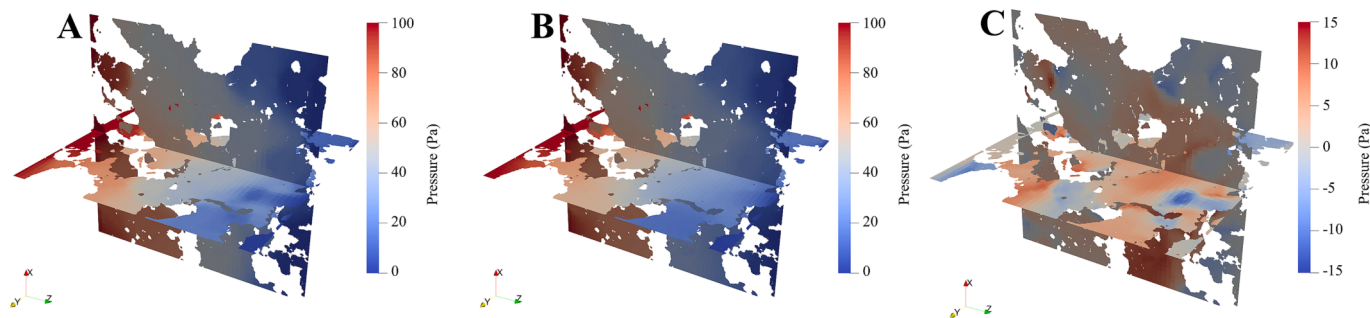


Fig. 14. Pressure distributions (A) in case 1 and (B) in case 2, as well as (C) the distribution of pressure difference between the two cases.

to over-coarsening of regions with strong variations of microporosity properties (e.g., porosity and pore size), which may cause errors in the numerical predictions. Physics-based coarsening methods may need to be developed to address this shortcoming. Finally, the accuracy of the present model relies on characterization of microporosity properties. Future studies will be focused on multiscale imaging and integration of microporosity flow parameters into a representative multiscale digital rock.

CRediT authorship contribution statement

Bowen Shi: Formal analysis, Software, Validation, Writing – original draft. **Han Jiang:** Investigation, Software, Validation. **Bo Guo:** Conceptualization, Methodology, Writing – review & editing. **Jian Tian:** Formal analysis, Investigation. **Chao-Zhong Qin:** Conceptualization, Funding acquisition, Methodology, Supervision, Writing – review & editing.

Declaration of competing interest

The authors declare that they have no known competing financial interests or personal relationships that could have appeared to influence the work reported in this paper.

Data availability

Data will be made available on request.

Acknowledgements

This work is supported by the National Natural Science Foundation of China (No. 12072053). HJ acknowledges the support of China Postdoctoral Science Foundation (No. 2022M720554). The image of Berea sandstone was obtain from (<https://www.imperial.ac.uk/earth-science/research/research-groups/pore-scale-modelling/micro-ct-images-and-networks/berea-sandstone/>). The datasets of Estaillades Carbonate sample were obtained through the Digital Rock Portal (<https://www.digitalrockportal.org/projects/363>). The dataset associated with the present work is available via 10.6084/m9.figshare.24117471.

References

- Aarnes, J.E., Gimse, T., & Lie, K.-A. (2007). An Introduction to the Numerics of Flow in Porous Media using Matlab. In: *Geometric Modelling, Numerical Simulation, and Optimization* (pp. 265–306).
- Alyafei, N., Blunt, M.J., 2016. The effect of wettability on capillary trapping in carbonates. *Adv. Water Resour.* 90, 36–50. <https://doi.org/10.1016/j.advwatres.2016.02.001>.
- Andrew, M., Bijeljic, B., Blunt, M.J., 2014. Pore-scale imaging of trapped supercritical carbon dioxide in sandstones and carbonates. *Int. J. Greenhouse Gas Control* 22, 1–14. <https://doi.org/10.1016/j.ijggc.2013.12.018>.
- Bauer, D., Youssef, S., Fleury, M., Bekri, S., Rosenberg, E., Vizika, O., 2012. Improving the estimations of petrophysical transport behavior of carbonate rocks using a dual pore network approach combined with computed microtomography. *Transp. Porous Media* 94 (2), 505–524. <https://doi.org/10.1007/s11242-012-9941-z>.
- Bijeljic, B., Mostaghimi, P., Blunt, M.J., 2013. Insights into non-fickian solute transport in carbonates. *Water Resour. Res.* 49 (5), 2714–2728. <https://doi.org/10.1002/wrcr.20238>.
- Blunt, M.J., Bijeljic, B., Dong, H., Gharbi, O., Iglesias, S., Mostaghimi, P., Pentland, C., 2013. Pore-scale imaging and modelling. *Adv. Water Resour.* 51, 197–216. <https://doi.org/10.1016/j.advwatres.2012.03.003>.
- Bultreys, T., Van Hoorebeke, L., Cnudde, V., 2015. Multi-scale, micro-computed tomography-based pore network models to simulate drainage in heterogeneous rocks. *Adv. Water Resour.* 78, 36–49. <https://doi.org/10.1016/j.advwatres.2015.02.003>.
- Carrillo, F.J., Soulaine, C., Bourg, I.C., 2022. The impact of sub-resolution porosity on numerical simulations of multiphase flow. *Adv. Water Resour.* 161 <https://doi.org/10.1016/j.advwatres.2021.104094>.
- Chen, S., Qin, C., Guo, B., 2020. Fully implicit dynamic pore-network modeling of two-phase flow and phase change in porous media. *Water Resour. Res.* 56 (11) <https://doi.org/10.1029/2020wr028510>.
- Dai, J., Li, L., Lei, S., Yuting, J., Yukun, C., Shenghao, W., Chaozhong, Q., 2023. Limiting pathways and breakthrough pressure for CO₂ flow in mudstones. *J. Hydrol.* 625 <https://doi.org/10.1016/j.jhydrol.2023.129998>.
- Dautray, J., Bornert, M., Gland, N., Dimanov, A., Raphanel, J., 2011. Localized deformation induced by heterogeneities in porous carbonate analysed by multi-scale digital image correlation. *Tectonophysics* 503 (1–2), 100–116. <https://doi.org/10.1016/j.tecto.2010.09.025>.
- de Vries, E.T., Raoof, A., van Genuchten, M.T., 2017. Multiscale modelling of dual-porosity porous media; a computational pore-scale study for flow and solute transport. *Adv. Water Resour.* 105, 82–95. <https://doi.org/10.1016/j.advwatres.2017.04.013>.
- Dong, H., Blunt, M.J., 2009. Pore-network extraction from micro-computerized-tomography images. *Phys Rev E Stat Nonlin Soft Matter Phys* 80 (3 Pt 2), 036307. <https://doi.org/10.1103/PhysRevE.80.036307>.
- Duan, L., Sun, H., Zhang, L., Jin, Z., Fan, D., He, Y., Yao, J., 2022. A method for pore-scale simulation of single-phase shale oil flow based on three-dimensional digital cores with hybrid mineral phases. *Phys. Fluids* 34 (6). <https://doi.org/10.1063/5.0095965>.
- Fan, Y., Liu, K., Yu, L., Liu, J., Regenauer-Lieb, K., 2022. Assessment of multi-scale pore structures and pore connectivity domains of marine shales by fractal dimensions and correlation lengths. *Fuel* 330. <https://doi.org/10.1016/j.fuel.2022.125463>.
- Fischer, A., Eidel, B., 2020. Error analysis for quadtree-type mesh coarsening algorithms adapted to pixelized heterogeneous microstructures. *Comput. Mech.* 65 (6), 1467–1491. <https://doi.org/10.1007/s00466-020-01830-4>.
- Friskin, S.F., Perry, R.N., 2002. Simple and efficient traversal methods for quadtrees and octrees. *Journal of Graphics Tools* 7 (3), 1–11. <https://doi.org/10.1080/10867651.2002.10487560>.
- Gackiewicz, B., Lamorski, K., Slawinski, C., Hsu, S.Y., Chang, L.C., 2021. An intercomparison of the pore network to the navier-stokes modeling approach applied for saturated conductivity estimation from X-ray CT images. *Sci. Rep.* 11 (1), 5859. <https://doi.org/10.1038/s41598-021-85325-z>.
- Gharehdaghi, B., Price, J.S., Rezanezhad, F., Quinton, W.L., 2018. Evaluating the hydraulic and transport properties of peat soil using pore network modeling and X-ray micro computed tomography. *J. Hydrol.* 561, 494–508. <https://doi.org/10.1016/j.jhydrol.2018.04.007>.
- Gostick, J.T., 2017. Versatile and efficient pore network extraction method using marker-based watershed segmentation. *Phys. Rev. E* 96 (2–1), 023307. <https://doi.org/10.1103/PhysRevE.96.023307>.
- Gote, A., Fischer, A., Zhang, C., Eidel, B., 2022. Computational homogenization of concrete in the cyber-size-resolution-discretization (SRD) parameter space. *Finite Elem. Anal. Des.* 198 <https://doi.org/10.1016/j.finel.2021.103653>.
- Guo, B., Ma, L., Tchelepi, H.A., 2018. Image-based micro-continuum model for gas flow in organic-rich shale rock. *Adv. Water Resour.* 122, 70–84. <https://doi.org/10.1016/j.advwatres.2018.10.004>.
- Guo, B., Mehmani, Y., Tchelepi, H.A., 2019. Multiscale formulation of pore-scale compressible darcy-stokes flow. *J. Comput. Phys.* 397 <https://doi.org/10.1016/j.jcp.2019.07.047>.
- Jacob, A., Peltz, M., Hale, S., Enzmann, F., Moravcova, O., Warr, L.N., Kersten, M., 2021. Simulating permeability reduction by clay mineral nanopores in a tight sandstone by

- combining computer X-ray microtomography and focussed ion beam scanning electron microscopy imaging. *Solid Earth* 12 (1), 1–14. <https://doi.org/10.5194/se-12-1-2021>.
- Jangda, Z., Menke, H., Busch, A., Geiger, S., Bultreys, T., Lewis, H., Singh, K., 2022. Pore-scale visualization of hydrogen storage in a sandstone at subsurface pressure and temperature conditions: trapping, dissolution and wettability. *J. Colloid Interface Sci* 629 (Pt B), 316–325. <https://doi.org/10.1016/j.jcis.2022.09.082>.
- Jiang, Z., van Dijke, M.I.J., Sorbie, K.S., Couples, G.D., 2013. Representation of multiscale heterogeneity via multiscale pore networks. *Water Resour. Res.* 49 (9), 5437–5449. <https://doi.org/10.1002/wrcr.20304>.
- Karimi-Fard, M., Durlofsky, L.J., & Aziz, K. (2004). An Efficient Discrete-Fracture Model Applicable for General-Purpose Reservoir Simulators. *SPE Journal*, 9(02), 227-236 % @ 1086-1055X. 10.2118/88812-pa.
- Katz, A.J., Thompson, A.H., 1986. Quantitative prediction of permeability in porous rock. *Phys Rev B Condens Matter* 34 (11), 8179–8181. <https://doi.org/10.1103/physrevb.34.8179>.
- Khan, F., Enzmann, F., Kersten, M., Wiegmann, A., Steiner, K., 2011. 3D simulation of the permeability tensor in a soil aggregate on basis of nanotomographic imaging and LBE solver. *J. Soil. Sediment.* 12 (1), 86–96. <https://doi.org/10.1007/s11368-011-0435-3>.
- Leigrain, G., Cartraud, P., Perreard, I., Moës, N., 2011. An X-FEM and level set computational approach for image-based modelling: application to homogenization. *Int. J. Numer. Meth. Eng.* 86 (7), 915–934. <https://doi.org/10.1002/nme.3085>.
- Li, Y., Zha, M., Song, R., Aplin, A.C., Bowen, L., Wang, X., Zhang, Y., 2021. Microstructure and pore systems of shallow-buried fluvial mudstone caprocks in zhanhua depression, East China inferred from SEM and MICP. *Mar. Pet. Geol.* 132 <https://doi.org/10.1016/j.marpetgeo.2021.105189>.
- Lindquist, W.B., Lee, S.-M., Coker, D.A., Jones, K.W., Spanne, P., 1996. Medial axis analysis of void structure in three-dimensional tomographic images of porous media. *J. Geophys. Res. Solid Earth* 101 (B4), 8297–8310. <https://doi.org/10.1029/95jb03039>.
- Ma, L., Fauchille, A.-L., Ansari, H., Chandler, M., Ashby, P., Taylor, K., Lee, P.D., 2021. Linking multi-scale 3D microstructure to potential enhanced natural gas recovery and subsurface CO₂ storage for bowland shale, UK. *Energ. Environ. Sci.* 14 (8), 4481–4498. <https://doi.org/10.1039/d0ee03651j>.
- Ma, L., Gao, D., Qian, J., Han, D., Xing, K., Ma, H., Deng, Y., 2023. Multiscale fractures integrated equivalent porous media method for simulating flow and solute transport in fracture-matrix system. *J. Hydrol.* 617 <https://doi.org/10.1016/j.jhydrol.2022.128845>.
- Maire, E., 2003. X-ray tomography applied to the characterization of cellular materials. related finite element modeling problems. *Compos. Sci. Technol.* 63 (16), 2431–2443. [https://doi.org/10.1016/s0266-3538\(03\)00276-8](https://doi.org/10.1016/s0266-3538(03)00276-8).
- Mehmani, A., Prodanović, M., 2014. The effect of microporosity on transport properties in porous media. *Adv. Water Resour.* 63, 104–119. <https://doi.org/10.1016/j.advwatres.2013.10.009>.
- Nie, R.-S., Zhou, J., Chen, Z., Liu, J., Pan, Y., 2021. Pore structure characterization of tight sandstones via a novel integrated method: a case study of the sulige gas field, Ordos Basin (northern China). *J. Asian Earth Sci.* 213 <https://doi.org/10.1016/j.jseaes.2021.104739>.
- Olshanskii, M.A., Terekhov, K.M., Vassilevski, Y.V., 2013. An octree-based solver for the incompressible navier-stokes equations with enhanced stability and low dissipation. *Comput. Fluids* 84, 231–246. <https://doi.org/10.1016/j.compfluid.2013.04.027>.
- Qin, C.Z., Hassanzadeh, S.M., Ebigbo, A., 2016. Pore-scale network modeling of microbially induced calcium carbonate precipitation: insight into scale dependence of biogeochemical reaction rates. *Water Resour. Res.* 52 (11), 8794–8810. <https://doi.org/10.1002/2016wr019128>.
- Qin, C.Z., van Brummelen, H., Hefny, M., Zhao, J., 2021a. Image-based modeling of spontaneous imbibition in porous media by a dynamic pore network model. *Adv. Water Resour.* 152 <https://doi.org/10.1016/j.advwatres.2021.103932>.
- Qin, C.Z., Wang, X., Hefny, M., Zhao, J., Chen, S., Guo, B., 2022. Wetting dynamics of spontaneous imbibition in porous media: from pore scale to darcy scale. *Geophys. Res. Lett.* 49 (4) <https://doi.org/10.1029/2021gl097269>.
- Qin, Y., Yao, S., Xiao, H., Cao, J., Hu, W., Sun, L., Liu, X., 2021b. Pore structure and connectivity of tight sandstone reservoirs in petroleum basins: a review and application of new methodologies to the late triassic Ordos Basin, China. *Mar. Pet. Geol.* 129 <https://doi.org/10.1016/j.marpetgeo.2021.105084>.
- Rabbani, A., Jamshidi, S., Salehi, S., 2014. An automated simple algorithm for realistic pore network extraction from micro-tomography images. *J. Pet. Sci. Eng.* 123, 164–171. <https://doi.org/10.1016/j.petrol.2014.08.020>.
- Rabbani, A., Babaei, M., Javadpour, F., 2020. A triple pore network model (T-PNM) for gas flow simulation in fractured, micro-porous and meso-porous media. *Transp. Porous Media* 132 (3), 707–740. <https://doi.org/10.1007/s11242-020-01409-w>.
- Raeini, A.Q., Blunt, M.J., Bijeljic, B., 2014. Direct simulations of two-phase flow on micro-CT images of porous media and upscaling of pore-scale forces. *Adv. Water Resour.* 74, 116–126. <https://doi.org/10.1016/j.advwatres.2014.08.012>.
- Ruspini, L.C., Øren, P.E., Berg, S., Masalmeh, S., Bultreys, T., Taberner, C., Wilson, O.B., 2021. Multiscale digital rock analysis for complex rocks. *Transp. Porous Media* 139 (2), 301–325. <https://doi.org/10.1007/s11242-021-01667-2>.
- Shah, S.M., Gray, F., Crawshaw, J.P., Boek, E.S., 2016. Micro-computed tomography pore-scale study of flow in porous media: effect of voxel resolution. *Adv. Water Resour.* 95, 276–287. <https://doi.org/10.1016/j.advwatres.2015.07.012>.
- Silin, D.B., Jin, G., Patzek, T.W., 2003. Robust determination of the pore space morphology in sedimentary rocks. Paper Presented at the SPE Annual Technical Conference and Exhibition.
- Soulaine, C., Gjetvaj, F., Garing, C., Roman, S., Russian, A., Gouze, P., Tchelepi, H.A., 2016. The impact of sub-resolution porosity of X-ray microtomography images on the permeability. *Transp. Porous Media* 113 (1), 227–243. <https://doi.org/10.1007/s11242-016-0690-2>.
- Soulaine, C., Tchelepi, H.A., 2016. Micro-continuum approach for pore-scale simulation of subsurface processes. *Transp. Porous Media* 113 (3), 431–456. <https://doi.org/10.1007/s11242-016-0701-3>.
- Tanino, Y., Blunt, M.J., 2012. Capillary trapping in sandstones and carbonates: dependence on pore structure. *Water Resour. Res.* 48 (8) <https://doi.org/10.1029/2011wr011712>.
- Verhoosel, C.V., van Zwieten, G.J., van Rietbergen, B., de Borst, R., 2015. Image-based goal-oriented adaptive isogeometric analysis with application to the micro-mechanical modeling of trabecular bone. *Comput. Methods Appl. Mech. Eng.* 284, 138–164. <https://doi.org/10.1016/j.cma.2014.07.009>.
- Wang, S., Ruspini, L.C., Øren, P.E., Van Offenwert, S., Bultreys, T., 2022. Anchoring multi-scale models to Micron-scale imaging of multiphase flow in rocks. *Water Resour. Res.* 58 (1) <https://doi.org/10.1029/2021wr030870>.
- Weishaupt, K., Helmig, R., 2021. A dynamic and fully implicit non-isothermal, two-phase, two-component pore-network model coupled to single-phase free flow for the pore-scale description of evaporation processes. *Water Resour. Res.* 57 (4) <https://doi.org/10.1029/2020wr028772>.
- Wildenschild, D., Sheppard, A.P., 2013. X-ray imaging and analysis techniques for quantifying pore-scale structure and processes in subsurface porous medium systems. *Adv. Water Resour.* 51, 217–246. <https://doi.org/10.1016/j.advwatres.2012.07.018>.
- Wu, Y., Tahmasebi, P., Liu, K., Fagbemi, S., Lin, C., An, S., Ren, L., 2022. Two-phase flow in heterogeneous porous media: a multiscale digital model approach. *Int. J. Heat Mass Transf.* 194 <https://doi.org/10.1016/j.ijheatmasstransfer.2022.123080>.
- Xu, R., 2022. Flow capacity characterization of unconventional natural gas bearing rocks using digital rock physics: a comparison between advection and diffusion. *J. Pet. Sci. Eng.* 215 <https://doi.org/10.1016/j.petrol.2022.110624>.
- Yang, Y., Yao, J., Wang, C., Gao, Y., Zhang, Q., An, S., Song, W., 2015. New pore space characterization method of shale matrix formation by considering organic and inorganic pores. *J. Nat. Gas Sci. Eng.* 27, 496–503. <https://doi.org/10.1016/j.jngse.2015.08.017>.
- Yang, Y., Wang, K., Zhang, L., Sun, H., Zhang, K., Ma, J., 2019. Pore-scale simulation of shale oil flow based on pore network model. *Fuel* 251, 683–692. <https://doi.org/10.1016/j.fuel.2019.03.083>.
- Zhang, L., Guo, B., & Xiong, Y. (2019). *A novel hybrid nano-continuum modeling framework for the transport processes in kerogen*.
- Zhang, L., Guo, B., Qin, C., Xiong, Y., 2023. A hybrid pore network-continuum modeling framework for flow and transport in 3D digital images of porous media. *EarthArxiv e-Prints*. <https://doi.org/10.31223/X5QT1K>.
- Zhao, J., Qin, F., Derome, D., Carmeliet, J., 2020. Simulation of quasi-static drainage displacement in porous media on pore-scale: coupling lattice boltzmann method and pore network model. *J. Hydrol.* 588 <https://doi.org/10.1016/j.jhydrol.2020.125080>.